Three-Dimensional Simulations of Biofilm Growth in Porous Media

D. A. Graf von der Schulenburg and T. R. R. Pintelon
Dept. of Chemical Engineering, University of Cambridge, Pembroke Street, Cambridge CB2 3RA, U.K.

C. Picioreanu and M. C. M. Van Loosdrecht
Dept. of Biotechnology, Delft University of Technology, Julianalaan 67, 2628 BC, Delft, The Netherlands

M. L. Johns
Dept. of Chemical Engineering, University of Cambridge, Pembroke Street, Cambridge CB2 3RA, U.K.

DOI 10.1002/aic.11674
Published online December 29, 2008 in Wiley InterScience (www.interscience.wiley.com).

Biofilm growth occurs in a variety of random porous media in a range of industrial processes; prediction of its growth and subsequent influence on hydrodynamics is hence desirable. In this study, we present the first numerical 3D pore-scale model of biofilm growth in porous media, based on a lattice Boltzmann simulation platform complemented with an individual-based biofilm model (IbM). We use it to explore the coupled interaction between nutrient mass transport, biofilm growth, and hydrodynamics. Biofilm is shown to be very effective at reducing the permeability of porous media, particularly under nutrient limited conditions. We conclude with a direct comparison of 3D and 2D biofilm growth simulations in porous media and show the necessity of performing the simulations in 3D.
 AIChE J, 55: 494–504, 2009
Keywords: biofilm, growth model, 3D, lattice Boltzmann, porous media, hydrodynamics, mass transport

Introduction

Microorganisms such as bacteria attach to a variety of surfaces, such as metals, plastics, stone, or tissue, and embed themselves via an extracellular polymeric substance (EPS) by which they form spatially heterogeneous structures collectively called biofilms. Such biofilm growth within porous media is of particular importance in a variety of industrial scenarios such as biofilm-mediated soil filtration, biofilm growth during oil recovery,[1] paper manufacturing and food processing operations,[2] membrane biofouling,[3] bioremediation processes, and biofilm growth in water treatment and heat exchange systems.[4] Because of the importance of biofilm growth in random porous media, a variety of experimental studies have appeared in the literature,[5–13] aimed primarily at improving our understanding of the interaction of biofilm growth and porous media hydrodynamics. To complement and extend such studies, suitable 3D modeling/simulation of biofilm growth in such complex support structures is desirable.

A variety of 1D, 2D, and 3D models of general biofilm growth have been developed and reported in the literature (see Wanner et al.[14] for an overview). Because of the spatial heterogeneity of both biofilms and the support structure provided by the porous media, 3D modeling is very desirable. Biofilm growth models reported in the literature generally feature simplifications (usually justifiably introduced to improve computational speed) that make them unsuitable for porous media applications. Often the influence of hydrodynamics is excluded and/or biofilm is modeled as a 2D system. These models enable studies of the impact of antimicrobials,[15] biofilm detachment mechanisms,[16] biofilm structure,[17] and biofilm pattern formation,[18] albeit on a flat support structure. A variety of 2D and 3D models have

Correspondence concerning this article should be addressed to M. L. Johns at mlj21@cam.ac.uk.

appeared in the literature[17,19] that include hydrodynamics and simulate biofilm growth on a flat surface. Direct coupling of mass transfer and hydrodynamics with biofilm growth in porous media has only been reported for 2D support structures.[20–22]

Here we present a 3D numerical simulation of biofilm growth within a random porous medium that includes coupled hydrodynamics, nutrient mass transport, and their interaction with biofilm growth. The lattice Boltzmann (LB) method was used to solve the coupled hydrodynamics and subsequent mass transport equations of dissolved nutrients (e.g., oxygen), because of its proven high performance in simulating these processes in any arbitrary complex geometry.[23] The fluid velocity, pressure, and solute concentrations fields calculated with LB were then coupled with an individual based biofilm growth model (IbM)[24–26] and, as such, are an extension of an algorithm previously used for 2D cellular automata biofilm growth models.[17] To the best of our knowledge, this is the first report of a 3D model of biofilm growth in porous media. This modeling platform is used to quantify permeability reduction in response to biofilm growth and highlight the necessity of using 3D simulations of the biofilm growth.

Model Formulation

The computational domain is a box with liquid inlet on one face, liquid outlet on the opposite face, and the other faces being non-periodic solid wall boundary conditions. The microscale model for the porous medium contains three phases: the liquid in the pore space, the biofilm growing on the solid carrier, and the solid carrier particles (e.g., sand). Because the solid phase is assumed neither permeable to the transported solutes nor to liquid, model equations are written for only two computational sub-domains: pore liquid and biofilm.

The model needs to describe hydrodynamics through the porous structure, mass transfer of solute nutrients, and subsequent biofilm growth. This initially necessitates solution of the equations of continuity (Eq. 1) and the Navier-Stokes momentum balance (Eq. 2) in 3D, for an incompressible Newtonian liquid flowing through the pore space or the porous medium:

$$\nabla \mathbf{u} = 0 \tag{1}$$

$$\frac{\partial \mathbf{u}}{\partial t} + \mathbf{u}\nabla\mathbf{u} = -\frac{1}{\rho}\nabla p + v\nabla^2\mathbf{u}, \tag{2}$$

with $\mathbf{u}$, the local velocity vector, p the pressure, ρ the local density, and v the kinematic viscosity of the liquid. All simulations were run with a constant flow rate during biofilm growth, which was imposed by a constant inlet velocity and constant outlet pressure boundary condition (see Table 1 for velocity values). At the biofilm-liquid and at the solid-liquid interfaces, no-slip wall conditions ($\mathbf{u} = 0$) are assumed.

Mass transport of nutrient solutes includes advective transport coupled with Fickian diffusion and a reactive source/sink term, r_s:

$$\frac{\partial C_s}{\partial t} + \mathbf{u}\nabla C_s - D_s\nabla^2 C_s = r_s, \tag{3}$$

where C_s is the local concentration of the species s (e.g., a nutrient for the micro-organisms, referred to as a "substrate"), with diffusivity, D_s. Equation 3 is applied in the pore space sub-domain without the reaction term r_S, because we assume negligible substrate consumption by planktonic bacteria (suspended in the liquid). In the biofilm sub-domain, the advection term from Eq. 3 is neglected because we assume diffusion to be the most important mass transport mechanism in the biofilm matrix. The consumption of a single substrate (e.g., oxygen) by the biofilm is described by Monod kinetics[27]:

$$r_s = -q_{\max} C_x \frac{C_s}{K_s + C_s}, \tag{4}$$

where C_x is the local biomass concentration, $q_{\max}$ the maximum specific uptake rate, and K_s the half-saturation coefficient for that substrate. The growth rate of biomass is then described by:

$$\frac{dC_x}{dt} = -Y_{xs} r_s, \tag{5}$$

where Y_{xs} is the growth yield. The mechanism of biofilm accumulation, which leads to C_x, from the growth of individual microorganisms with mass m_x is described below. The boundary conditions for Eq. 3 are: constant concentration in the inlet ($C_S = C_{S0}$) and zero diffusive flux in the outlet ($\partial C_S/\partial z = 0$). Zero-flux (impermeability) conditions are also applied at the solid-fluid interface. Mass flux continuity conditions apply at the biofilm-liquid interfaces.

Table 1. Simulation Parameters Used

Simulation	Inlet Velocity u_0 (m/s)	Inlet Substrate Concentration C_{s0} (kg/m^3)	$q_{\max}$ (1/day)	Geometry
Sim1	1.0×10^{-4}	1.0×10^{-2}	10	Geom1
Sim2	1.0×10^{-4}	3.0×10^{-4}	10	Geom1
Sim3	1.0×10^{-4}	3.0×10^{-4}	10	Geom2
Sim4	1.0×10^{-4}	1.0×10^{-2}	5	Geom1
Sim5	5.0×10^{-5}	3.0×10^{-4}	10	Geom1

Simulation Strategy

The first computational step is to solve the hydrodynamics using the LB method (see Figure 1). The resulting velocity field of liquid flowing between the solid components of the porous medium is then used to simulate the mass transport of different chemical species (e.g., nutrients, oxygen, or products) consumed or produced by different bacteria based on a biomass concentration field. The resulting fields of solute concentration are thus used by the IbM model component to simulate the growth of the biofilm. These computational steps provide new biomass concentration fields and a new input geometry to distinguish the biofilm sub-domain from free liquid for the next iteration of the LB computations.

The algorithm thus decouples hydrodynamics and mass transport from biofilm growth. This approach may be used due to the differences in time scales of these processes.[17] A flow field adapts very rapidly to new geometries (~seconds), whereas biofilm growth occurs on much slower time scale (~days). For the sake of simplicity, this approach ignores interactions between biofilm and the flow field that occur on

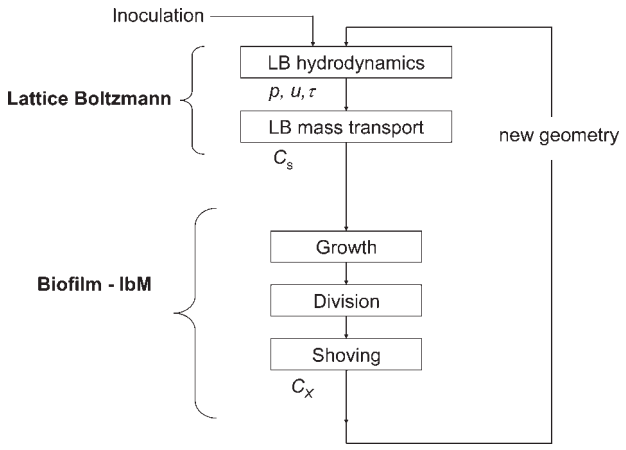

Figure 1. The general algorithm combines hydrodynamics, mass transport, biomass growth, and biomass spreading processes.

The initial values of the flow velocity field, **u,** and nutrient concentration, C_s, are relaxed iteratively to pseudo-steady states. After this, biomass concentration C_x changes in the biofilm-related algorithm steps. Because the biofilm geometry has changed, the whole cycle is iterated. The computational duration of one iteration for a 120 pixel^3 porous media was ~10 h on a single processor.

similar time scales; such as shear induced biofilm deformation, filamentous streamer formation,[28] or biofilm detachment (the shear rates simulated are too small to effect detachment in any case). Inclusion of such interactions will be the subject of future work.

Lattice Boltzman method

The single value relaxation Bhatnagar-Gross-Krook LB method[29] was used to simulate the 3D pore scale flow field. The method models the hydrodynamics of a fluid on a mesoscopic scale, where fluid kinetics are described by probability distribution functions $f_i(\mathbf{x},t)$ of the location of particles, $\mathbf{x}$. These functions move with a velocity, $\mathbf{c}_i$, on a discrete lattice (with Δx the distance between nodes) through a discrete evolving time, Δt. The collision of particles is governed by relaxation of $f_i(\mathbf{x},t)$ towards equilibrium, $f_i^{\mathrm{eq}}(\mathbf{x},t)$:

$$f_i(\mathbf{x}+\mathbf{c}_i, t+1) - f_i(\mathbf{x},t) = -\frac{1}{\tau}\left(f_i(\mathbf{x},t) - f_i^{\mathrm{eq}}(\mathbf{x},t)\right), \quad (6)$$

where τ is the Bhatnagar-Gross-Krook[30] relaxation parameter and the equilibrium function depends on the local particle density, ρ, and particle momentum, $\bar{\rho}\mathbf{u}$, for each lattice direction i ($i = 1,2,3 \ldots 19$)

$$\rho = \sum_i f_i(\mathbf{x},t) \quad (7)$$

$$\overline{\rho}\mathbf{u} = \sum_i f_i(\mathbf{x},t)\mathbf{c}_i. \quad (8)$$

The particle momentum in Eq. 8 allows the calculation of the local velocity values, $\mathbf{u}$. τ depends on the lattice kinematic viscosity,

$$v = \frac{1}{3}\left(\tau - \frac{1}{2}\right) \quad (9)$$

The corresponding equilibrium function reads[31]

$$f_i^{\mathrm{eq}}(\rho,\mathbf{u};\mathbf{x},t) = \rho A_i + \overline{\rho}(B_i\mathbf{c}_i\mathbf{u} + C_i\mathbf{c}_i^2\mathbf{u}^2 + D_i\mathbf{u}^2) \quad (10)$$

A_i, B_i, C_i and D_i are constant coefficients and the equations of continuity (Eq. 1) and Navier-Stokes (Eq. 2) can be generated from the equations above for certain values for these constants (dependant upon lattice geometry) by applying a Taylor expansion to the left hand side of Eq. 6 and a Chapman-Enskog expansion to its right hand side.[29,32] In this study, a nonslip boundary condition at the fluid solid interface is implemented; the method is second-order accurate and computationally inexpensive.[33]

The mass transport LB method is based on the model proposed by Flekkøy[34] and each chemical species s is tracked using a similar form to Eq. 6:

$$f_{i,\mathrm{s}}(\mathbf{x}+\mathbf{c},t+1) - f_{i,\mathrm{s}}(\mathbf{x},t) = -\frac{1}{\kappa_{\mathrm{s}}}\left(f_{i,\mathrm{s}}(\mathbf{x},t) - f_{i,\mathrm{s}}^{\mathrm{eq}}(\mathbf{x},t)\right), \quad (11)$$

where κ_{s} is the relevant relaxation parameter and depends on the species' diffusivity

$$D = 2J_{i,\mathrm{s}}\left(\kappa_{\mathrm{s}} - \frac{1}{2}\right) \quad (12)$$

The equilibrium function is defined as:

$$f_{i,\mathrm{s}}^{\mathrm{eq}}(C_{\mathrm{s}},\mathbf{u},\mathbf{x},t) = C_{\mathrm{s}}(J_{i,\mathrm{s}} + E_i\mathbf{c}_i\cdot\mathbf{u}). \quad (13)$$

$J_{i,\mathrm{s}}$ and E_{s} are constant coefficients. Each species is considered a fully miscible solute able to be advected and diffused within the carrier solvent (but only diffused and not advected within the biofilm). Again by Taylor and Chapman-Enskog expansions of the time dependent Eq. 11 using the equilibrium distribution, Eq. 13, one can obtain the macroscopic advection-diffusion reaction equation (Eq. 3).

More details on the LB method used in this study and on its experimental and analytical validation can be found in the literature for both the hydrodynamics[35–38] and the mass transport components.[39–41]

Individual based biofilm growth model (IbM)

Although the LB method is based on a discrete grid, the individual-based biofilm model uses continuous Cartesian space in 3D. Individual and immotile cells are assumed to be spheres of variable properties (e.g., volume, mass, kinetic properties). They undergo growth, division and spreading (as outlined in Figure 1). Initially cells are inoculated by placement at random positions on the substratum surface (the support grains). The cells consume nutrients and grow according to Eqs. 4 and 5. If the biomass exceeds a defined maximum biomass, the cell divides into a mother and a daughter cell, each consisting of a fraction of the initial total cell mass, close to 0.5 but uniformly randomly chosen. After division cells are spread out to maintain a minimum distance between cells.[24–26] The overlapping radii, $R_0 = k_{\mathrm{e}} \times R_{\mathrm{A}} + R_{\mathrm{B}} - d_{\mathrm{e}}$, between two neighboring cells A and B with radii R_{A} and R_{B} is calculated using the Euclidean distance, d_{e}, between the center position of A and B. The shoving parameter, k_{e}, enables the adjustment of the minimum distance between

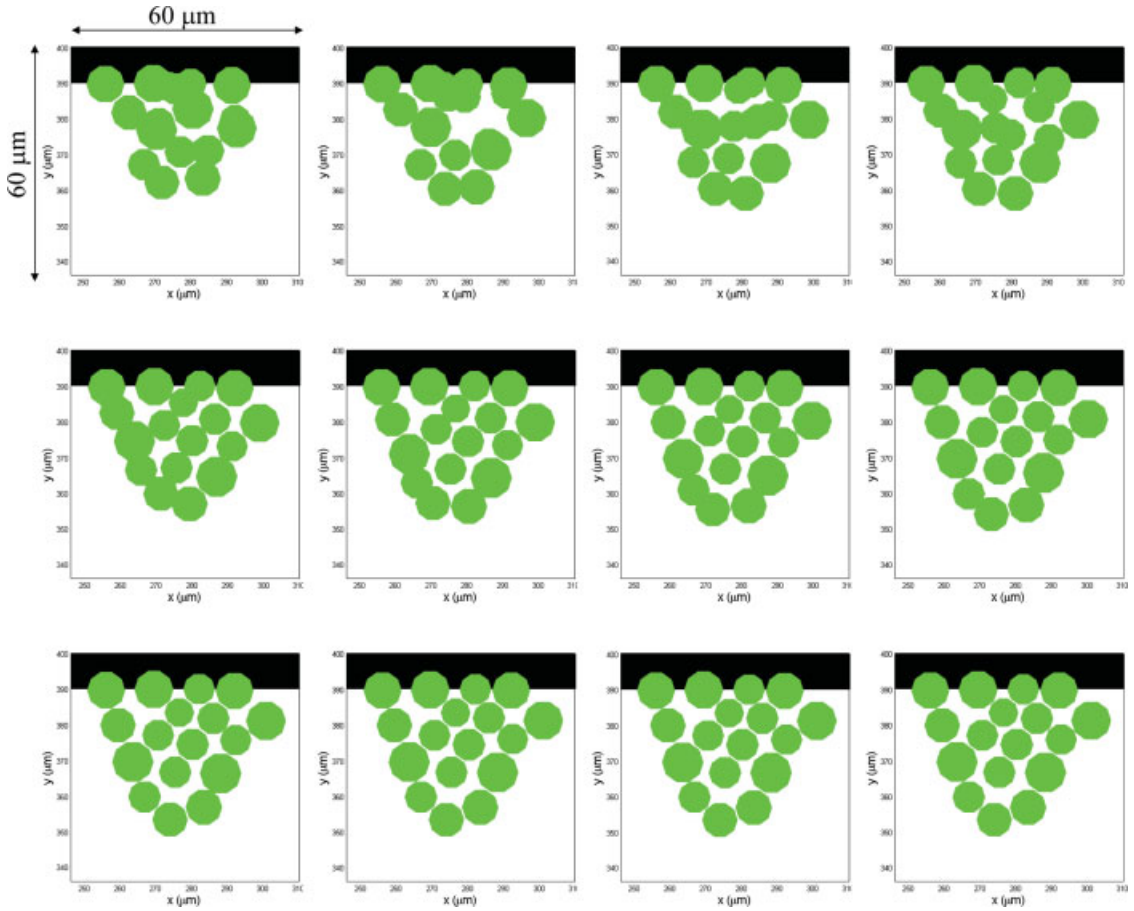

Figure 2. A simulation of the shoving principle for a small colony of 17 overlapping cells in 2D.

In this example, the cell radii vary between 3.7 and 5.9 μm and shoving parameter k_e is unity. Cells are addressed one by one and moved to a new position according to the shoving vector. This is repeated until all cells reach the minimum shoving distance. In the shown example 12 shoving iterations are necessary. [Color figure can be viewed in the online issue, which is available at www.interscience.wiley.com.]

neighboring cells (shove radius). The vector sum of all positive R_0 for all cells neighboring one cell is calculated and the center of that cell is shifted in the negative direction of the vector sum (shoving vector). This is done for all cells and repeated iteratively until the shove radius is achieved between all cells. Figure 2 shows a simulation of the shoving principle for a small colony of 17 overlapping cells in 2D. In this example, the cell radii vary between 3.7 and 5.9 μm and shoving parameter k_e is unity. Cells are addressed one by one and moved to a new position according to the shoving vector. This is repeated until all cells reach the minimum shoving distance. In the example shown, 12 shoving iterations are necessary. For more details on the spreading algorithm, the following literature[24–26] is recommended.

Simulation Parameters

Hydrodynamics and solute transport sub-models

All 3D simulations were done on a domain of 2400 $\times$ 2400 $\times$ 2400 μm^3 discretized on a LB matrix of 120 $\times$ 120 $\times$ 120 nodes with an isotropic resolution, $\Delta x = 20$ μm. The matrix including the discretized distribution of solid and liquid in the porous medium was obtained via magnetic resonance imaging of a saturated random packing of glass beads.[42] The mean size of the beads in the simulation matrix was 400 μm. D_s was the diffusion coefficient of oxygen in water at room temperature (2.0×10^{-9} m^2/s) and viscosity v was chosen for water (1.0×10^{-6} m^2/s). Dissolved oxygen is often the limiting growth factor in aerobic biofilms.[43] The time step, Δt, for both the hydrodynamic and the mass transport simulations where chosen to obtain $\tau \sim 1$ and $\kappa_s \sim 0.505$ to have the highest possible simulation accuracy.[40] The packed bed matrix had a porosity of $\varepsilon_1 = 0.59$ (Geom1). A second geometry was created by using an erosion algorithm[42] to Geom1. The erosion algorithm converts all solid pixels neighboring a fluid pixel into a fluid pixel. This was done to obtain a second geometry (Geom2) with a higher porosity, $\varepsilon_2 = 0.72$, to study the influence of packing porosity on biofilm growth without altering the porous media structure significantly.

Biofilm sub-model

6000 cells were randomly initialized with an initial cell mass of 1.0×10^{-11} g on the surface of the carrier beads. The maximum cell mass at which cells divide was 2.0 $\times$

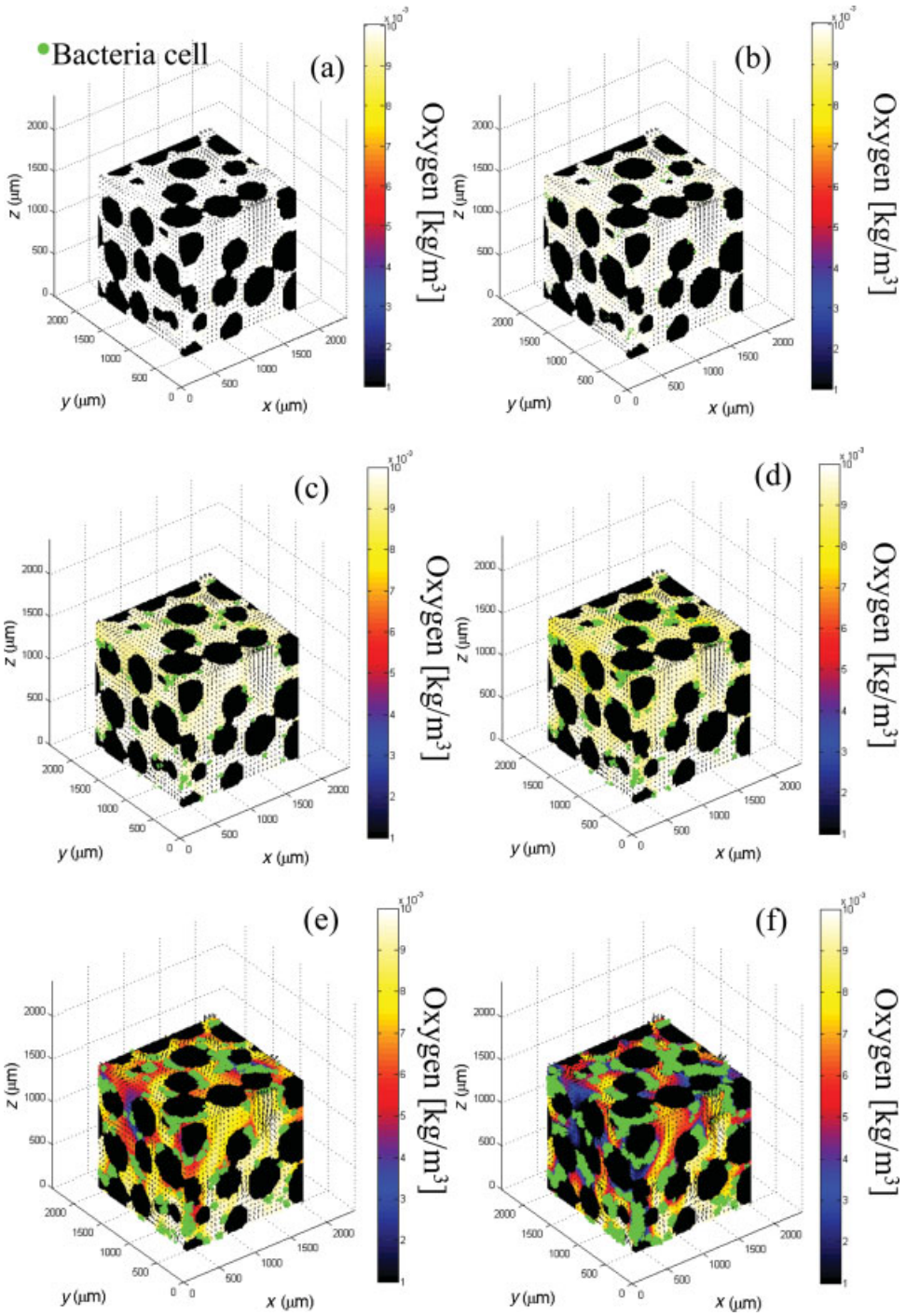

Figure 3. 3D cut away views of a typical biofilm growth simulation in porous media for 0 (a), 9 (b), 12 (c), 13.5 (d), 16.5 (e), and 18 h (f) of biofilm growth.

Bacteria are shown as green spheres. The flow field is from bottom to top and shown by black velocity vectors. The oxygen concentration is indicated by the color scale in kg/m^3. The simulation corresponds to Geom1 and Sim1 as described in Table 1. [Color figure can be viewed in the online issue, which is available at www.interscience.wiley.com.]

10^{-11} g (corresponding to a 7.2 μm cell radius). The shoving parameter, k_e, was set equal to 1.0 and the number of maximum shoving iterations was 100. The duration of a biofilm growth step was 1.5 h. The stoichiometric ratio biomass:substrate was $Y_{xs} = 0.5$ kg biomass/kg substrate, and the half-saturation coefficient was $K_s = 0.1$ kg/m^3. The inlet velocity u_0, the inlet nutrient concentration, C_{s0}, and the maximum specific substrate uptake rate q_{max} were varied in a series of

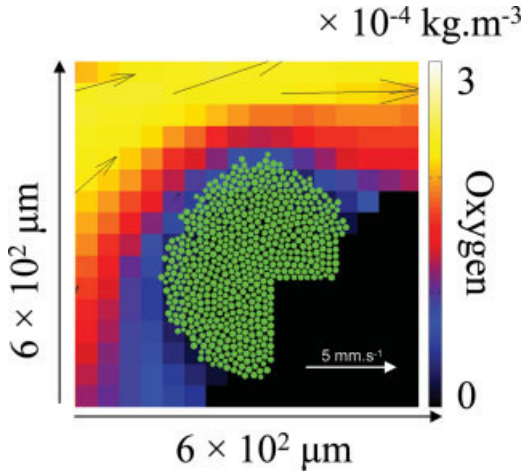

Figure 4. Example of a 2D porous model system.

The flow field direction is from left to right and is visualized by black velocity vectors (a velocity scale is shown). Nutrient concentration is indicated by the color scale in kg/m^3. Biofilm cells are represented by green spheres attached to the solid substratum beads shown in black. [Color figure can be viewed in the online issue, which is available at www.interscience.wiley.com.]

simulations as detailed in Table 1. Parameters were selected for the simulations to match those commonly measured for oxygen consumption.[44]

For the 2D simulations, a *z*-*y* slice was extracted from the 3D geometry, Geom1 (at an *x*-position of 700 μm). See Figure 3a for a definition of the Cartesian coordinates *x*, *y*, and *z*. Inoculation was identical to Geom1 as were all relevant simulation parameters. The porosity of the 2D slice (0.58) is very similar to that of Geom1 (0.59).

Results and Discussion

3D simulation

A sample set of simulations are presented in Figure 3, corresponding to Geom 1 and Sim1 as described in Table 1. Figures 3a–f show cut-away views (from all 3 directions) of the system: (a) after inoculation (0 h) and after (b) 9, (c) 12 (d) 13.5 (e) 16.5, and (f) 18 h of biofilm growth. The superficial flow direction is in the vertical axial (*z*) direction. Bacteria are shown as green spheres, the local flow vectors are shown using black arrows and the color scale indicates the local dissolved O_2 (nutrient) content. The progression seen through Figure 3a–f is as expected; biofilm accumulation increases both the heterogeneity and magnitude of the velocity field whilst depleting the nutrient (O_2) concentration field and increasing its heterogeneity. Figure 4 shows a two-dimensional closer view of a typical biofilm colony obtained on the surface of the support beads.

From the temporally resolved 3D data, as presented in Figure 3, we are able to extract out the temporal evolution in various macroscopic characteristics of the system for the range of simulations outlined in Table 1. Figure 5a shows the increase in biofilm mass in the system over time for Sim1-5. The influence of a high inlet nutrient concentration is evident in Sim1 where biomass accumulation is significantly more rapid than in Sim2. Comparing Sim2 and Sim3 reveals that the higher porosity in Sim3 results in a slightly larger accumulation rate of biomass. This is a consequence of both the larger total nutrient supply (due to the higher porosity) and of the reduction in flow field heterogeneity. Comparison of Sim1 and Sim4 reveals that the simulations are acutely sensitive to q_{max}, the maximum growth rate for the range of conditions selected. Sim5 features a smaller input velocity than Sim2 and consequently a slightly reduced rate of biofilm accumulation.

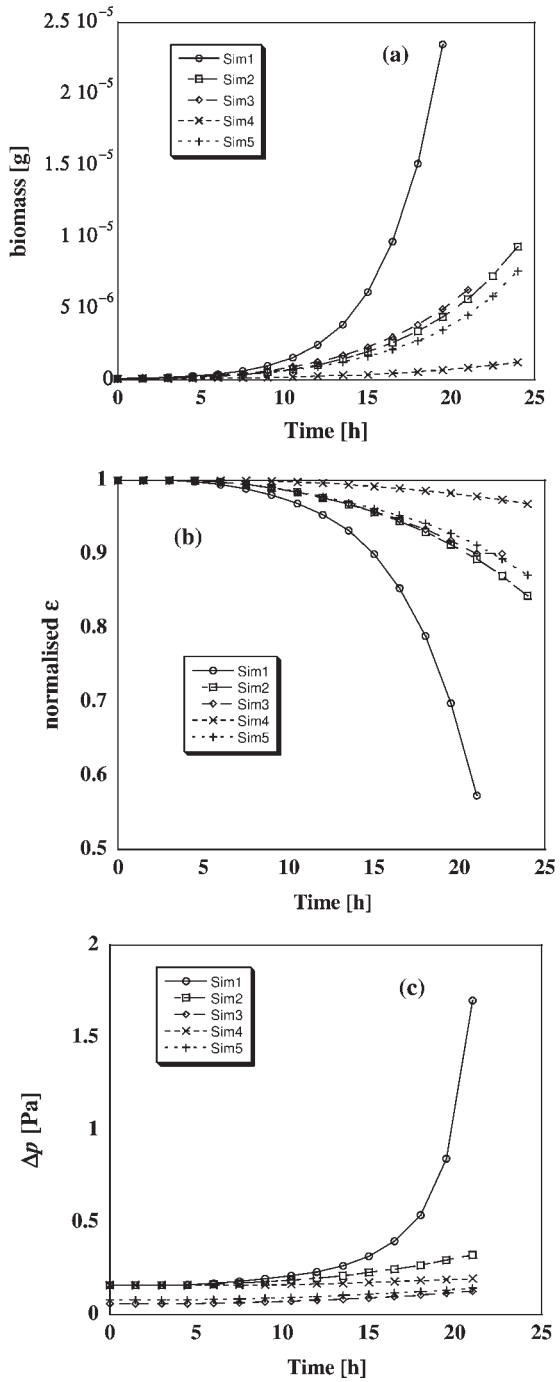

Figure 5. Development of biomass (a), normalized ε (b), and Δp (c) in time during the 3D biofilm growth simulations.

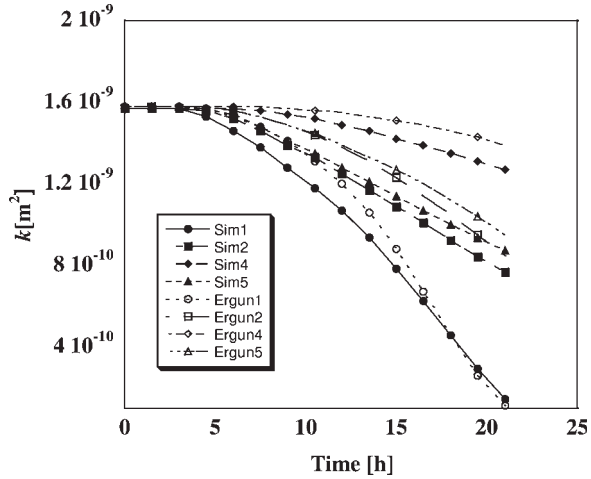

Figure 6. Development of *k* with time during the 3D biofilm growth simulation and according to the Ergun equation (Eq. 15).

The biofilm growth shown in Figure 5a reduces the bulk liquid pore volume, V_p, in the porous media. This decreases the porosity, $\varepsilon = V_p/(V_p + V_s + V_b)$, where V_s is the volume of solid carrier spheres and, V_b, the volume filled with biomass (as shown in Figure 5b for Sim1 to Sim5) and leads to an increase in pressure drop, Δp, determined across the simulation domain (as shown in Figure 5c). We can use the resultant values of Δp to extract the porous media permeability, k, using Darcy's equation[45]

$$k = -\frac{Q\mu L}{A\Delta p}, \tag{14}$$

which depends on the total flow rate, Q, through cross-sectional area, A, the dynamic viscosity, and the system length, L.

Δp can be obtained directly from the LB simulation or estimated using the Ergun equation,[45] typically used to describe the correlation between ε and Δp in random spherical packings with sphere diameter, d,

$$\frac{\Delta p}{L} = 150\left(\frac{\mu u_z}{d^2}\right)\frac{(1-\varepsilon)^2}{\varepsilon^3} + \frac{7}{4}\left(\frac{\rho u_z^2}{d}\right)\frac{1-\varepsilon}{\varepsilon^3}. \tag{15}$$

The resultant evolution in the permeability, k, of the system in response to biofilm growth and hence reduction in effective porosity, ε, is presented in Figure 6 for all simulations described in Table 1, as determined from the LB simulations and as predicted by Eq. 15. The general trends of the evolution of k with time/biofilm growth is in qualitative agreement with experimental observations for biofilm growth in packed bed geometries.[46] Agreement between the simulation and Eq. 15 is excellent with respect to no or insignificant biofilm accumulation. As biofilm accumulated however, the simulations systematically predict a smaller value of k than that estimated by Eq. 15. Biofilm growth is an effective mechanism for "clogging" up such geometries when nutrient supply is limited; this can be advantageous (e.g., formation of subsurface barriers) or disadvantageous (e.g., fouling of bio-

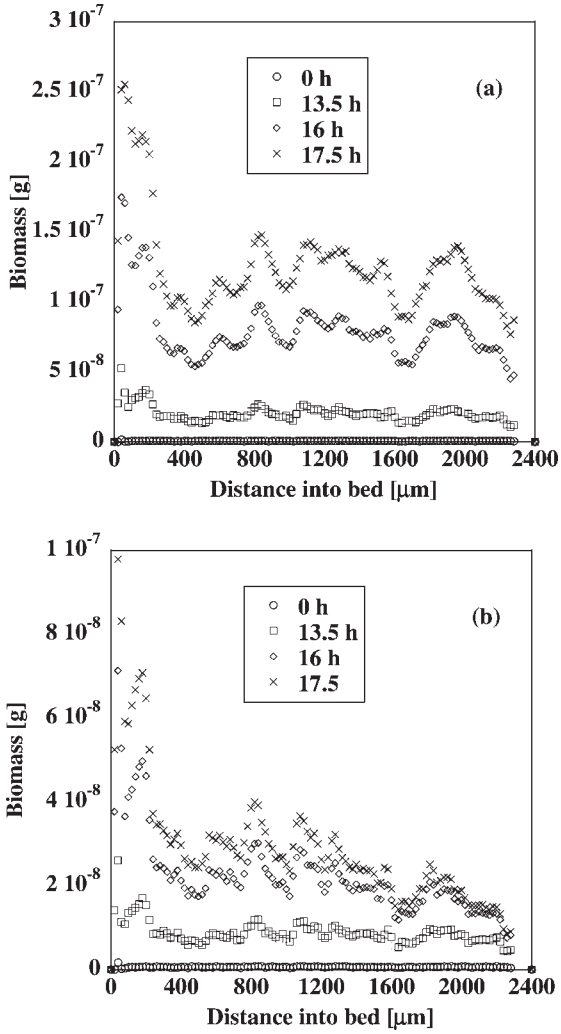

Figure 7. Change of total biomass with axial distance into the bed in time for a higher (Figure 7(a): Sim1) and lower inlet concentration (Figure (7(b): Sim2).

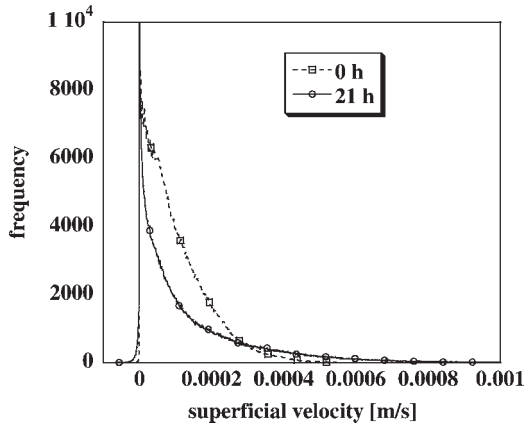

Figure 8. Comparison of u_z distribution before and after 21 h of biofilm growth according to Sim1 and Geom1, as described in Table 1.

reactors). In high velocity channels of the pore space, biofilm growth is encouraged by the enhanced nutrient supply and consequently flowrate through that channel is reduced due to enhanced biofilm accumulation. Overall permeability is more influenced by such channels and their effective reduction in both number and cross-sectional area means that a small amount of biofilm growth can have a significant influence on permeability. This is only true for nutrient limited systems,

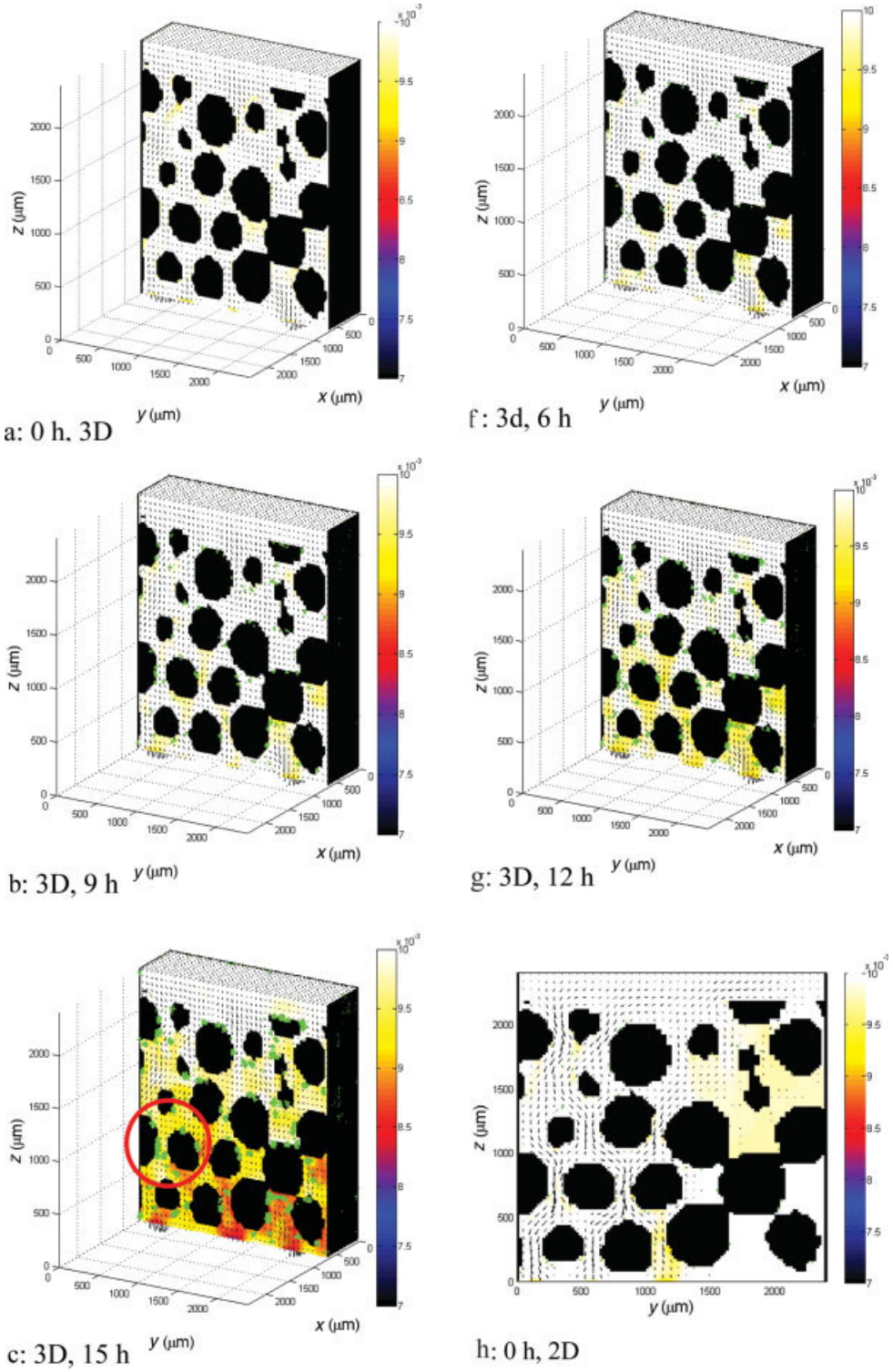

Figure 9. Comparisons of 3D simulation (Sim1) (a–e) with the 2D simulation (f–j) for the time steps 0, 6, 9, 12, 15 h after inoculation.

For the 3D simulation the same slice is shown that was used as an input geometry for the 2D simulation. The scalebar refers to O_2 concentration (kg/m^3). [Color figure can be viewed in the online issue, which is available at www.interscience.wiley.com.]

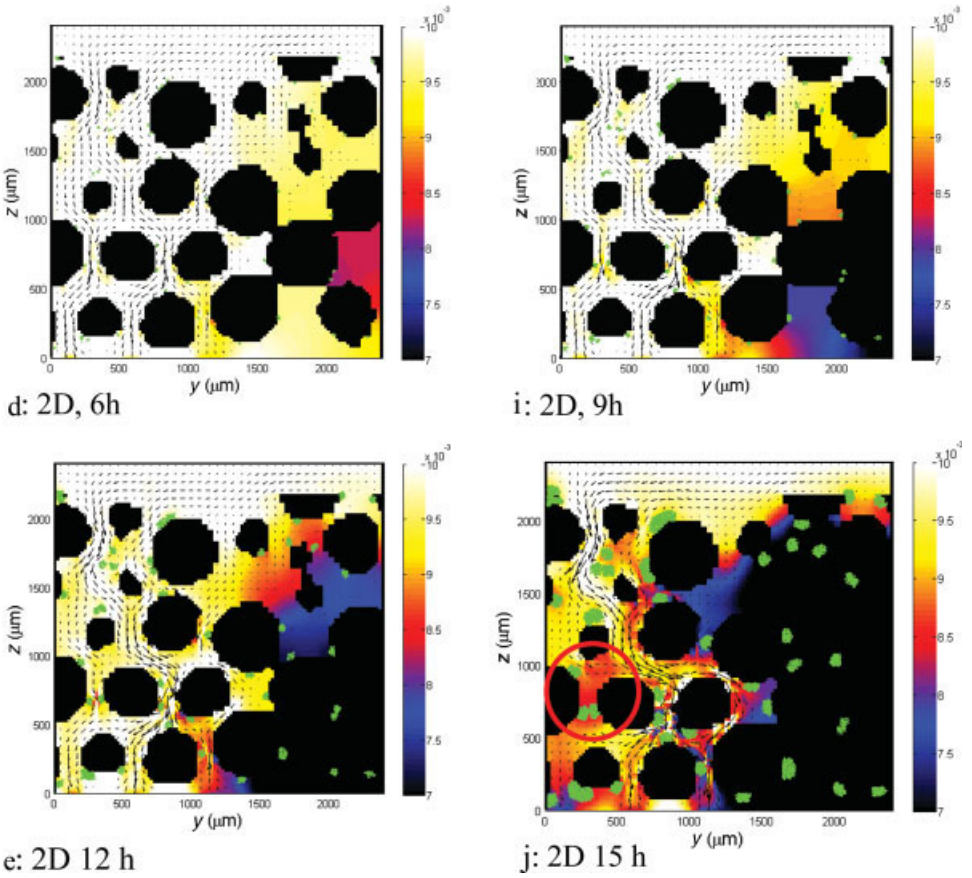

Figure 9. (Continued from the previous page)

and the effect will be reduced when shear-induced detachment of biofilm is considered (as mentioned previously, this is not relevant for the flow rates considered here). Biofilm is consequently a potentially effective medium for reducing permeability in fractured or very heterogeneous porous media structures.

Figure 7 shows the change of total biomass as a function of axial (z) distance into the simulation matrix as a function of time for (a) a higher (Sim1) and (b) lower (Sim2) nutrient inlet concentration. In both cases, biofilm accumulation occurs preferentially closer to the inlet. This is in qualitative agreement with experimental observations of biofilm growth in a range of systems.[46,47] For the lower inlet concentration (Figure 7b), a steeper biomass gradient is established along z, which suggests that the biomass gradient is introduced by nutrient limitation through the bed.

Figure 8 shows the superficial velocity, u_z, distributions of the flow for simulation Sim1 before and 21 h after inoculation. Note that these distributions were calculated excluding the solid, biofilm and ~0 velocity pixels. The velocity distribution becomes more heterogeneous with biofilm growth with increasing stagnant regions (peak around zero velocity) and fast channels (bigger tail for higher velocities). The velocity standard deviation increases from 8.64×10^{-5} m/s to 1.6×10^{-4} m/s. These trends are qualitatively consistent with experimental observations.[48]

Comparison of 2D and 3D simulation

Figure 9 compares a slice from the 3D simulation (Sim1) (a–e) with a 2D simulation on the same extracted slice (f–j) for the times at 0, 6, 9, 12, 15 h after inoculation. Differences between the 2D and 3D simulations are immediately evident: the nutrient and velocity fields in the 2D simulations

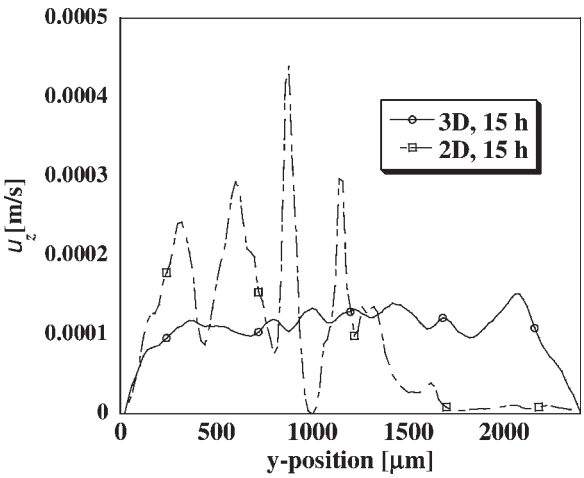

Figure 10. Mean velocity distributions (in *y* direction) for the 3D and 2D simulation after 15 h.

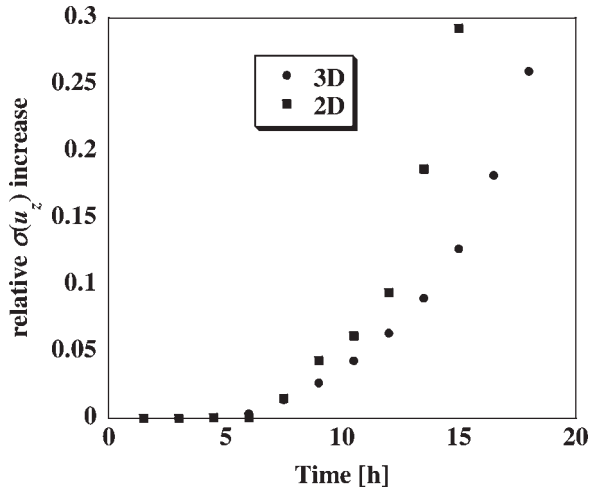

Figure 11. The development of $\sigma(u_z)$ with time for both 2D and 3D simulations.

become significantly more heterogeneous over time when compared with the 3D simulations. In 2D, a closed pore neck (e.g., due to touching solids or biofilm clogging) will immediately prevent advection in that region and the comparatively much slower diffusive flux will yield low nutrient concentration due to consumption. In 3D, the greater connectivity means that a closed pore neck due to biofilm growth is unlikely to lead to a stagnant region as nutrient advective flow will penetrate from the third dimension. Such an event is highlighted by the red circles in Figure 9.

Given an operation with a constant volumetric flow rate during biofilm growth (as in the simulations conducted here), use of a 2D simulation matrix will result in enhanced pore space clogging and a consequential increase in velocity heterogeneity. This is evident at a number of locations in Figure 9. Figure 10 shows the mean velocity as a function of transverse position (y) for both the 2D and 3D (same slice) simulations after 15 h for Sim1 conditions; the greater heterogeneity of the 2D simulations is immediately obvious. The velocity distribution in the 3D case is remarkably homogeneous and indicates that finger formation is suppressed in such systems. The superficial velocity standard deviation, $\sigma(u_z)$ presented in Figure 11, increases significantly faster in 2D than in 3D (note that the system was completely clogged after 15 h for the 2D simulation). We conclude that to accurately predict biofouling and its effect on hydrodynamics in porous media, 3D simulations are necessary. Eberl et al.[19] compared 2D and 3D simulations of biofilm growth on a flat support surface. Although biofilm shape irregularities were not the same in 2D and 3D, the correlation between nutrient supply and biofilm surface area increase due to growth was consistent for 2D and 3D simulations. Clearly, one cannot extrapolate these results to the porous medium systems considered here.

Conclusions

We have presented the first 3D numerical pore-scale model of biofilm growth in porous media. The numerical model allows the calculation of the velocity, pressure, and nutrient concentration fields, as well as the biomass distribution and porous media permeability. The qualitative trends of these variables are in agreement with experimental observations. Comparison of the simulation predictions of permeability as a function of biofilm accumulation when compared with estimation of this relationship using Ergun's equation revealed the effectiveness of biofilm accumulation at reducing the permeability of porous media. We have further compared 3D and 2D simulations and shown that 2D simulations in porous media are not capable of accurately describing the biofouling process. Future work will focus on including a biofilm detachment mechanism based on local shear rate and including bacterial attachment. This will hopefully enable a systematic study leading to a predictive capacity of permeability reduction due to biofilm accumulation.

Notation

A = column area (m^2)
A_i, B_i, C_i, D_i = LB constant coefficients for direction i
E_s = LB constant coefficients for species s
C_s = local concentration of a solute species (e.g., substrate) (kg solute/m^3)
C_x = local biomass concentration (kg biomass/m^3biofilm)
c_i = particle velocity
D_s = diffusion coefficient of solute (m^2/s)
d_e = Euclidean distance (m)
$f_i(x,t)$ = LB probability function for direction i
$f_i^{eq}(\mathbf{x},t)$ = LB equilibrium function for direction i
K_s = half-saturation coefficient (kg solute/m^3)
k_e = shoving parameter
k = porous media permeability (m^2)
L = system length (m)
$J_{i,s}$ = LB constant coefficients for species s and direction i
p = pressure (N/m^2)
Δp = pressure drop (N/m^2)
Q = volumetric flow rate (m^3/s)
q_{max} = maximum specific substrate uptake rate (kg solute/kg biomass s)
R_0 = overlapping radii between cells (m)
R_A, R_B = radii of neighboring cells A and B (m)
r_s = reaction rate for solute substrate (kg solute/m^3s)
t = time (s)
Δt = time step size (s)
u = velocity vector (m/s)
$u_{z,inter}$ = mean superficial interstitial velocity (m/s)
V_p = pore volume (m^3)
V_s = volume of solid spheres (m^3)
V_b = the volume filled with biomass (m^3)
Y_{xs} = growth yield (kg biomass/kg substrate)
x = location of particles (m)
Δx = pixel (mesh) size (m)
ε = porosity (m^3 liquid/m^3 total space)
κ_s = diffusivity-correlated relaxation parameter for species s
μ = liquid dynamic viscosity (Pa s)
ν = liquid kinematic viscosity (m^2/s)
ρ = liquid density (kg/m^3)
$\bar{\rho}\mathbf{u}$ = particle momentum
τ = Bhatnagar-Gross-Krook relaxation parameter

Literature Cited

1. Head IM, Jones DM, Larter SR. Biological activity in the deep subsurface and the origin of heavy oil. *Nature* 2003;426:344–352.
2. Wong ACL. Biofilms in food processing environments. *J Dairy Sci*. 1998;81:2765–2770.
3. Flemming HC. Reverse osmosis membrane biofouling. *Exp Therm Fluid Sci*. 1997;14:382–391.
4. Bott TR. Techniques for reducing the amount of biocide necessary to counteract the effects of biofilm growth in cooling water systems. *Appl Therm Eng*. 1998;18:1059–1066.

5. Taylor SW, Jaffe PR. Biofilm growth and the related changes in the physical-properties of a porous-medium. 1. *Exp Invest Water Resour Res*. 1990;26:2153–2159.
6. Taylor SW, Jaffe PR. Biofilm growth and the related changes in the physical-properties of a porous-medium. 3. *Dispersivity Model Verification Water Resour Res*. 1990;26:2171–2180.
7. Taylor SW, Jaffe PR. Substrate and biomass transport in a porous-medium. *Water Resour Res*. 1990;26:2181–2194.
8. Taylor SW, Milly PCD, Jaffe PR. Biofilm growth and the related changes in the physical-properties of a porous-medium. 2. *Permeability Water Resour Res*. 1990;26:2161–2169.
9. Vandevivere P, Baveye P. Improved preservation of bacterial exopolymers for scanning electron-microscopy. *J Microsci Oxford*. 1992;167:323–330.
10. Vandevivere P, Baveye P. Relationship between transport of bacteria and their clogging efficiency in sand columns. *Appl Environ Microbiol*. 1992;58:2523–2530.
11. Baveye P, Vandevivere P, Delozada D. Biofilm growth and the related changes in the physical-properties of a porous-medium. 1. *Exp Invest Comment Water Resour Res*. 1992;28:1481–1482.
12. Cunningham AB, Characklis WG, Abedeen F, Crawford D. Influence of biofilm accumulation on porous-media hydrodynamics. *Environ Sci Technol*. 1991;25:1305–1311.
13. Stewart TL, Folger SH. Pore-scale investigation of biomass plug development and propagation in porous media. *Biotechnol Bioeng*. 2002;77:577–588.
14. Wanner O, Eberl HJ, Morgenroth E, Noguera D, Picioreanu C, Rittmann BE, Van Loosdrecht MCM. Mathematical Modeling of Biofilms. IWA Scientific and Technical Report No. 18, IWA Publishing, 2006.
15. Chambless JD, Hunt SM, Stewart PS. A three-dimensional computer model of four hypothetical mechanisms protecting biofilms from antimicrobials. *Appl Environ Microbiol*. 2006;72:2005–2013.
16. Chambless JD, Stewart PS. A three-dimensional computer model analysis of three hypothetical biofilm detachment mechanisms. *Biotechnol Bioeng*. 2007;97:1573–1584.
17. Picioreanu C, van Loosdrecht MCM, Heijnen JJ. Effect of diffusive and convective substrate transport on biofilm structure formation: a two-dimensional modeling study. *Biotechnol Bioeng*. 2000;69:504–515.
18. Gonpot P, Smith R, Richter A. Diffusion limited biofilm growth. *Model Simul Mater Sci*. 2000;8:707–726.
19. Eberl HJ, Picioreanu C, Heijnen JJ, van Loosdrecht MCM. A three-dimensional numerical study on the correlation of spatial structure, hydrodynamic conditions, and mass transfer and conversion in biofilms. *Chem Eng Sci*. 2000;55:6209–6222.
20. Dillon R, Fauci L. A microscale model of bacterial and biofilm dynamics in porous media. *Biotechnol Bioeng*. 2000;68:536–547.
21. Kapellos GE, Alexiou TS, Payatakes AC. Hierarchical simulator of biofilm growth and dynamics in granular porous materials. *Adv Water Resour*. 2007;30:1648–1667.
22. Thullner M, Baveye P. Computational pore network modeling of the influence of biofilm permeability on bio-clogging in porous media. *Biotechnol Bioeng*. 2008;99:1337–1351.
23. Koponen A, Kataja M, Timonen J, Kandhai D. Simulations of single-fluid flow in porous media. *Int J Mod Phys C*. 1998;9:1505–1521.
24. Kreft JU, Booth G, Wimpenny JWT. BacSim, a simulator for individual-based modelling of bacterial colony growth. *Microbiol UK*. 1998;144:3275–3287.
25. Kreft JU, Picioreanu C, Wimpenny JWT, van Loosdrecht MCM. Individual-based modelling of biofilms. *Microbiol Sgm*. 2001;147:2897–2912.
26. Picioreanu C, Kreft JU, van Loosdrecht MCM. Particle-based multidimensional multispecies Biofilm model. *Appl Environ Microbiol*. 2004;70:3024–3040.
27. Beeftink HH, Vanderheijden RTJM, Heijnen JJ. Maintenance requirements—energy supply from simultaneous endogenous respiration and substrate consumption. *Fems Microbiol Ecol*. 1990;73:203–209.
28. Klapper I, Rupp CJ, Cargo R, Purvedorj B, Stoodley P. Viscoelastic fluid description of bacterial biofilm material properties. *Biotechnol Bioeng*. 2002;80:289–296.
29. Chen S, Doolen GD. Lattice Boltzmann method for fluid flows. *Annu Rev Fluid Mech*. 1998;30:329–364.
30. Qian YH, Dhumieres D, Lallemand P. Lattice Bgk models for Navier-stokes equation. *Europhys Lett*. 1992;17:479–484.
31. He XY, Luo LS. Lattice Boltzmann model for the incompressible Navier-Stokes equation. *J Stat Phys*. 1997;88:927–944.
32. Wolfram S. Cellular automata fluids 1: basic theory. *J Stat Phys*. 1986;3/4:471–526.
33. Gallivan MA, Noble DR, Georgiadis JG, Buckius RO. An evaluation of the bounce-back boundary condition for lattice Boltzmann simulations. *Int J Numer Methods Fluids*. 1997;25:249–263.
34. Flekkoy EG. Lattice Bhatnagar-Gross-Krook models for miscible fluids. *Phys Rev E*. 1993;47:4247–4257.
35. Manz B, Gladden LF, Warren PB. Flow and dispersion in porous media: Lattice-Boltzmann and NMR studies. *AIChE J*. 1999;45:1845–1854.
36. Mantle MD, Bijeljic B, Sederman AJ, Gladden LF. MRI velocimetry and Lattice-Boltzmann simulations of viscous flow of a Newtonian liquid through a dual porosity fibre array. *Magn Reson Imaging*. 2001;19:527–529.
37. Gladden LF, Alexander P, Britton MM, Mantle MD, Sederman AJ, Yuen EHL. In situ magnetic resonance measurement of conversion, hydrodynamics and mass transfer during single- and two-phase flow in fixed-bed reactors. *Magn Reson Imaging*. 2003;21:213–219.
38. Yuen EHL, Sederman AJ, Sani F, Alexander P, Gladden LF. Correlations between local conversion and hydrodynamics in a 3-D fixed-bed esterification process: an MRI and lattice-Boltzmann study. *Chem Eng Sci*. 2003;58:613–619.
39. Sullivan SP, Akpa BS, Matthews SM, Fisher AC, Gladden LF, Johns ML. Simulation of miscible diffusive mixing in microchannels. *Sens Actuators B*. 2007;123:1142–1152.
40. Sullivan SP, Sani FM, Johns ML, Gladden LF. Simulation of packed bed reactors using lattice Boltzmann methods. *Chem Eng Sci*. 2005;60:3405–3418.
41. Sullivan SP, Sederman AJ, Johns ML, Gladden LF. Verification of shear-thinning LB simulations in complex geometries. *J Non-Newtonian Fluid*. 2007;143:59–63.
42. Baldwin CA, Sederman AJ, Mantle MD, Alexander P, Gladden LF. Determination and characterization of the structure of a pore space from 3D volume images. *J Colloid Interface Sci*. 1996;181:79–92.
43. Jansen JL, Harremoes P. Removal of soluble substrates in fixed films. *Water Sci Technol*. 1985;17:1–14.
44. Characklis WG, Marshall KC. *Biofilms*. NJ: Wiley, 1990.
45. Bird RB, Warren ES, Lightfoot EN. *Transport Phenomena*. NC: Wiley, 2006.
46. Simoni SF, Schafer A, Harms H, Zehnder AJB. Factors affecting mass transfer limited biodegradation in saturated porous media. *J Contam Hydrol*. 2001;50:99–120.
47. Vrouwenvelder JS, van Paassen JAM, Wessels LP, van Dama AF, Bakker SM. The membrane fouling simulator: a practical tool for fouling prediction and control. *J Membr Sci*. 2006;281:316–324.
48. Seymour JD, Gage JP, Codd SL, Gerlach R. Anomalous fluid transport in porous media induced by biofilm growth. *Phys Rev Lett*. 2004;93:198103.

Manuscript received July 1, 2008, and revision received July 21, 2008.